

UNIVERSIDADE ESTADUAL DE CAMPINAS
SISTEMA DE BIBLIOTECAS DA UNICAMP
REPOSITÓRIO DA PRODUÇÃO CIENTÍFICA E INTELECTUAL DA UNICAMP

Versão do arquivo anexado / Version of attached file:

Versão do Editor / Published Version

Mais informações no site da editora / Further information on publisher's website:

<https://www.mdpi.com/1999-4907/13/11/1935>

DOI: <https://doi.org/10.3390/f13111935>

Direitos autorais / Publisher's copyright statement:

©2022 by MDPI. All rights reserved.

DIRETORIA DE TRATAMENTO DA INFORMAÇÃO

Cidade Universitária Zeferino Vaz Barão Geraldo

CEP 13083-970 – Campinas SP

Fone: (19) 3521-6493

<http://www.repositorio.unicamp.br>

Article

Tomographic Images Generated from Measurements in Standing Trees Using Ultrasound and Postprocessed Images: Methodological Proposals for Cutting Velocity, Interpolation Algorithm and Confusion Matrix Metrics Focusing on Image Quality

Stella S. S. A. Palma, Mariana N. dos Reis  and Raquel Gonçalves * 

FEAGRI, Unicamp—School of Agricultural Engineering, University of Campinas, Campinas 13083-875, Brazil

* Correspondence: raquelg@unicamp.br



Citation: Palma, S.S.A.; dos Reis, M.N.; Gonçalves, R. Tomographic Images Generated from Measurements in Standing Trees Using Ultrasound and Postprocessed Images: Methodological Proposals for Cutting Velocity, Interpolation Algorithm and Confusion Matrix Metrics Focusing on Image Quality. *Forests* **2022**, *13*, 1935. <https://doi.org/10.3390/f13111935>

Academic Editor: Brian Kane

Received: 17 October 2022

Accepted: 16 November 2022

Published: 17 November 2022

Publisher's Note: MDPI stays neutral with regard to jurisdictional claims in published maps and institutional affiliations.



Copyright: © 2022 by the authors. Licensee MDPI, Basel, Switzerland. This article is an open access article distributed under the terms and conditions of the Creative Commons Attribution (CC BY) license (<https://creativecommons.org/licenses/by/4.0/>).

Abstract: Tomographic images generated by wave propagation are important in tree inspections and can be performed in an economically more accessible way using conventional equipment and postprocessed images, but improvements are necessary to increase image quality, giving greater reliability to the results. The objective of this paper was to present a methodological proposal for the definition of parameters related to image quality produced with tomography using ultrasound equipment and postprocessed images. As a case study, the methodology was applied to five trees of the species *Cenostigma pluviosum* DC. Gagnon & GP Lewis (Sibipiruna). A total of 1512 tomographic images were constructed from five trees to evaluate the cutting velocity, the interpolation algorithms and the filter application. The photographs of the discs were used to evaluate the theoretical wave propagation routes in the measurement grid and to compare the tomographic images using confusion matrix metrics. The application of the methodology proposed in this species allowed us to conclude that the most appropriate velocity range for cavities inference was up to 40% V_{max} and for cavities supplemented with biodeterioration up to 45% V_{max} ; the best interpolator was the Ellipses method with compensation, with the use of a filter; and the accuracy was the most appropriate metric for evaluating image quality.

Keywords: confusion matrix; interpolation algorithms; tree inspection; image filters

1. Introduction

Trees are important elements in urban landscapes but require special care in the choice of appropriate species, the use of planting beds with sufficient growth space and the monitoring of their phytosanitary status [1]. Therefore, professionals involved in tree care should associate biological knowledge with technological tools to identify trees with the potential for structural failure [2]. Thus, in recent decades, less invasive tree inspection techniques have been the focus of researchers worldwide [3]. The growing interest in noninvasive inspection tools and extensive research in this area has allowed the development of commercial equipment using acoustic and electromagnetic wave propagation [3] and equipment based on mechanical microporations such as those based on drilling resistance. Of the wave propagation techniques, stress waves have been the most studied for applications in standing trees [4] and the most commonly used in commercial tomographs [3], but studies involving ultrasound wave applications [5–9] have demonstrated not only the viability of this technique but also some advantages, such as the ability to control the frequency to be used in the inspection. One of the major obstacles to the dissemination and use of acoustic tomography is equipment cost, which is high for some communities and urban forest managers. This paper is dedicated to presenting and discussing a methodology capable of fulfilling the need for a more affordable inspection

tool. However, because it is more simplified, it still needs specific studies to ensure its accuracy. On the other hand, industrialized equipment in general includes interpolation systems and more complex filters, which allow for higher image quality, a very important aspect for increasing the credibility of the technology. Thus, this article is part of broader research that extends knowledge to increase the quality of tomography generated with the use of conventional ultrasound equipment and simplified techniques in the construction of postprocessed images.

The images constructed with the simplified method proposed here use speed ranges associated with colors, which in turn can be associated with the health conditions of the wood. To obtain the velocity data, measurement meshes that allow scanning velocities are used inside the trunk under inspection, with the diffraction mesh (Figure 1) being one of the most common [10].

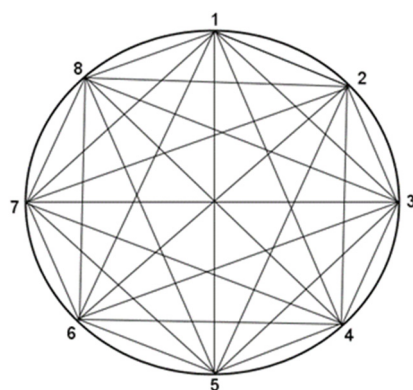


Figure 1. Example of an 8-point diffraction mesh.

For this scan, the mesh created between the measurement points forms the theoretical routes (Ex: 1–2, 1–3, etc.), in which the velocities are calculated by the relationship between the theoretical length of the route and the time for the wave to cover it (TOF). Thus, disregarding probable deviations in a simplified manner, wave propagation occurs in these routes [10], thereby passing through zones of healthy wood, zones of deteriorated wood or a mixture of both. In practice, deviations from this theoretical route occur for different reasons, such as impedance variations between the propagation media [11], singularities such as knots, pockets of resin and pith [12], moisture [11,13,14], wave tendency to seek the physical environment to propagate, bypassing void zones, such as cavities [15], and propagation direction, which in the case of a diffraction mesh can be radial or tangential with different angles [13].

However, regardless of the inspection mesh used, it is not possible to obtain velocity values for all points of a transversal section, and it is therefore necessary to use velocity interpolation algorithms [16–18]. The algorithm allows not only to fill out velocities outside the mesh, but also to adapt the behavior of the routes as a function of the type of interpolation used, as proposed by [17], which considers velocity compensations as a function of anisotropy, correcting the theoretical routes. Thus, the tomography result is influenced by both the characteristics of the mesh, such as the number of measurement points [19,20], and the type of interpolation algorithm; therefore, it is necessary to calibrate this interference for the correct interpretation of the tomographic image, especially in the case of using less complex interpolators.

Tomographic image quality can also be improved through filters. Filters applied directly to ultrasound tomography images are useful in reducing interference caused by interpolation systems [19]. However, the author's research [19] was carried out with simulated discs, and it is important to verify that the results are repeatable with real trunk cross-sections.

A confusion matrix is a tool used to quantitatively evaluate classification models and images [16]. In a binary confusion matrix, such as the one discussed in this paper, when

one wants to evaluate how close the produced image and the real image are, a zone of interest in the real image (called a model) is compared with the same zone of interest in the produced image (called *Roi* = region of interest) and these comparison metrics are used to quantify the quality of the images.

The choice of the most appropriate metric to evaluate how much a produced image is representative of the real image should be made according to what is to be evaluated or what is considered most important in an inspection.

Considering the importance of obtaining more objective information about the quality of tomography performed with conventional ultrasound equipment and simpler image construction techniques, the objective of this study was to present a methodological proposal applied to the species *Cenostigma pluviosum* (Sibipiruna) as a case study for the definition of parameters related to the images produced by this technique. The focus parameters of the study were the cutting speed ranges for the inference of cavities and cavities plus biodeteriorations, the interpolation algorithms, the use of filters to construct the image and the confusion matrix metrics.

2. Materials and Methods

2.1. Materials

For this study, five trees of the species *Cenostigma pluviosum* DC. Gagnon & GP Lewis (Sibipiruna), all located on the campus of the State University of Campinas, in the city of Campinas, State of São Paulo, Brazil (22°49'03" S 47°04'11" W), were used as case studies for the application of the methodological proposal.

Sibipiruna is a tree species of the Legume family located in several regions of Brazil. Because it has an ornamental canopy (Figure 2), it is one of the most cultivated native species in urban afforestation in Brazil, especially in the south-central part of the country. The trees of this species can reach 20 m in height, and their stems can have average diameters of the order of 50 cm. They have a shallow root system, scaly bark, dense canopy, umbelliform shape, semideciduous foliage and yellow flowers.



Figure 2. Example of a Sibipiruna tree with flower detail. Source: Adapted from <http://www.jardimcor.com/catalogo-de-especies/cenostigma-pluviosum/>, accessed on 10 January 2022.

Considering the species available for the study, Sibipiruna was chosen because it is abundant in Brazilian cities, in addition to being the species with the highest number of trees authorized to be cut for use in this study, allowing us to expand the sampling and choose specimens with different apparent types of trees through biodeterioration, a fundamental characteristic for research.

2.2. Methodology

2.2.1. Diffraction Mesh and Number of Measurement Points

A diffraction mesh [10] was adopted for tests on standing trees (Figure 1); however, it was necessary to adopt the number of measurement points. The calculation of the number of measurement points (n) in the diffraction mesh can be made as a function of the stem perimeter (P) in the section to be inspected [19]. These authors [19] concluded that the adoption of a number of measurements equal to five times the perimeter (in meters) allowed a balance between image quality and fieldwork. The number of measurement pointsline ($n = 5P$) must always be even to guarantee the existence of theoretical radial routes [19]. Thus, we initially measured, in the field, the perimeters of all sections where ultrasound measurements would be made. For each tree, three inspection heights (sections) were planned (at the base, at breast height ($\cong 1.3$ m) and at the height of the first bifurcation); however, for three trees the bifurcation heights were very close to the breast heights and so only two measurements were made (Table 1).

Table 1. Perimeter data of the stem sections where the trees were measured in the field and number of measurement points calculated.

Species	Tree	Section	Perimeter (m) (P)	Calculated Points of Measurement (n)	Approximate Measurement Points (n *)
Sibipiruna	1	1	2.52	13	14
		2	1.20	6	6
	2	1	1.48	7	8
		2	1.44	7	8
	3	1	1.10	6	6
		2	1.02	5	6
	4	1	1.60	8	8
		2	1.47	7	8
		3	1.47	7	8
	5	1	1.52	8	8
		2	1.48	7	8
		3	1.44	7	8
	Mean			7	8

Section: 1 = at the base, 2 = at the breast height ($\cong 1.3$ m), 3 = at the first bifurcation; * value calculated by the expression $n = 5 \times P$ approximated to the nearest n pair [19].

The stem sections had different perimeters, so the number of calculated measurement points also varied (Table 1). As the development of the research involved a series of comparisons, we considered it more appropriate to always adopt the same number of points in the inspections of standing trees, and then we assumed the mean, which was $n = 8$ points (Table 1).

2.2.2. Ultrasound Tests on Standing Trees

To mark the position of the eight measuring points, point 1 was adopted at one end of the section corresponding to the largest diameter. This point was used as a reference for the beginning of the inspection (diffraction mesh—Figure 1). To position the other measurement points, the perimeter of the stem in the inspection section was divided by $n = 8$. A hole of 5 mm in diameter was made at each point of the mesh with necessary depth to cross the bark so that the transducer would touch the wood, avoiding interference in wave propagation.

To read the wave propagation time, we used ultrasound equipment (USLab, Agricef®, Paulínia, Brazil) and a pair of transducers, one an emitter and the other a receiver, with exponential faces (dry tips) and 45 kHz frequency. The test started with the coupling of the emitter transducer at point 1 and the receiver transducer at point 2, forming theoretical

route 1–2 (Figure 1), and the wave propagation time was recorded manually. For the following readings, the emitting transducer remained at point 1, and the receiver traveled through the other points (2 to 8). Then, the emitter transducer was coupled to point 2, and the receiver was coupled to point 1, forming route 2–1 (Figure 1). The procedure was repeated until all readings in the routes were performed; thus, the wave propagation times were obtained in all routes.

2.2.3. Discs

After the trees were cut, discs were removed from the 12 sections of the stem where the ultrasound inspections of the standing tree had been performed. Using a process performed in another study by the group, the discs were polished, photographed and analyzed macroscopically and microscopically [21,22] to detail the cavities and biodeteriorations.

The software used in this study (*ImageWood*) to generate the tomographic images is noncommercial and was developed in 2015 with funding from a research organization in Brazil (São Paulo State Foundation—FAPESP) and has been improved over the years. It has already been validated externally by ad hoc advisors from FAPESP and also by reviewers of scientific papers in which it was used [5,19,21,22]. The software, better explained at item 2.2.4, was used to interpolate velocities obtained in the diffraction mesh (Figure 1) and two spreadsheets must be supplied for its use. One of the spreadsheets must have the coordinates (x, y) of the stem contour, and the other must have the coordinates of the initial (xi, yi) and final (xf, yf) points of the mesh measurement, associated with the wave propagation times measured by the equipment during field inspection. Obtaining the coordinates of the contour in standing trees is simple when the shape of the stem is regular, approaching a circle or an ellipse since mathematical approximations can be used. For irregular shafts, obtaining the coordinates is a more complex process, which can be performed with the use of lasers [23] or other techniques. In this stage of the research, because we had the discs, the contour coordinates were obtained in the open architecture software *ImageJ* using photographs of the discs. Initially, the largest diameter is marked on the surface of the disc, and then the disc is photographed. The image is then opened in the software, and its scale is transformed from pixels to centimeters with the *set scale* tool, using the largest diameter of known size as a base and as represented in the disc photo. Then, with the *multipoint* tool, the contour points are marked in the image sequentially (example in Figure 3) and clockwise, starting at point 1 as a reference in the initial measurement performed on the standing tree. The measurement points (marked in red in Figure 3) that correspond to the lengths obtained by dividing the perimeter by the number of measurement points adopted in this study as $n = 8$ are also marked. These points are saved in x and y coordinates in text that will be used to compose the outline worksheet.



Figure 3. Example of plotting of contour points (black) and measurement points (red) using *ImageJ* software.

The spreadsheet of the wave propagation time to be inserted in the image generation software is obtained by assigning the time data measured by the ultrasound equipment in each of the theoretical routes. The theoretical routes of the measurement grid (Figure 1) are obtained by combining the initial coordinates (x_i , y_i), corresponding to the measurement points where the emitting transducer was coupled, and final coordinates (x_f , y_f), corresponding to the measurement points where the receiver transducer was coupled.

2.2.4. Image Generation

ImageWood image processing software was used to generate the images. The spatial interpolation of the velocities was performed using two different interpolators: the inverse of the square of the distance (ISD) and the Ellipses method with and without velocity compensation proposed by [17]. The interpolator allows us to assign values of estimated velocity in regions where it is unknown from calculated velocities in the theoretical routes of measurement of the diffraction grid (Figure 1). The tomographic image is then generated by the association of colors to speed ranges, resulting in a color map that can be associated with wood biodeterioration conditions.

For image generation, it is also necessary to introduce the number of speed ranges and the associated colors in the software. Considering that the study used a binary confusion matrix to quantify the quality of the images, all images were constructed with only two colors. To establish the limit of the ranges of the velocities associated to the two colors, we used the maximum speed obtained in the inspection of each section as a reference value of the intact wood (without cavities or biodeteriorations). As previously noted, the ultrasound wave propagation speeds vary even in intact wood. However, in the presence of cavities or biodeteriorations, a reduction in velocity is expected at levels higher than those obtained as a result of the natural variability of the wood [4,24–26]. Thus, to infer the presence of cavities or biodeteriorations from the tomography image, it is necessary to know the level of reduction of the wave propagation speed expected in these regions. Considering that one of the objectives of this study was to propose a methodology for answering this question, the two-color images were constructed considering, for the inference of zones with cavities or deteriorations, increasing percentages (0% to 100% every 5%) of the maximum speed (V_{\max}).

Considering that the images generated using this simplified methodology show interference from the interpolation method, the study was performed by applying a filter to the images. The filter used (median with 25 neighboring pixels) was proposed by [19] for meshes with 8 measurement points.

2.2.5. Confusion Matrix

To quantitatively compare the images generated by tomography with photographs of the disc faces (real condition [21,22]), a binary confusion matrix was used. For comparison, the pixels that are within the zone of interest are considered positive, and those that are outside the area of interest are considered negative. Thus, from the comparison of the zone of interest in the produced image (*Roi*) with the zone of interest in the real image (*model*), four possible combinations are obtained [27], as shown in Table 2. The true positive (TP) means the correct indication by the tomographic image of a zone of interest of the *model*, and the true negative (TN) means the correct indication, by the tomographic image, of the nonexistence of the zone of interest in the model. Conversely, the false positive (FP) is the type I error and indicates that the tomographic image predicted the existence of a zone of interest that was not in the real image (*model*) and the false negative (FN) that the tomographic image did not predict the existence of a zone of interest (type II error) in the *model*.

Table 2. Situations produced comparing the zones of interest in the confusion matrix.

Zone of Interest in Real Image (Model)	Zone of Interest in Produced Image (Roi)	
	Zone of Interest Present	Zone of Interest Not Present
Zone of interest present	True positive (TP)	False negative (FN)
Zone of interest not present	False positive (FP)	True negative (TN)

The metrics of the confusion matrix have different criteria, and given their definitions, unless the image is accurate (all metrics equal to 100%), it is possible to have one metric with a high value while the others have low values. It is important to define which criterion is most appropriate for the inference of a specific condition that is to be evaluated by comparing the images.

Accuracy Equation (1) is a metric that defines the overall performance of the image; that is, how much of the zone of real interest (*model*) the produced image (*Roi*) correctly classified. In the example (Figure 4a), the accuracy was high because the produced image indicated the presence of the zone of interest with a dimension close to that of the model, even if the shape and position were not completely correct. In tree stem tomography, high accuracy, such as the example in Figure 4a, would be a good indicator of the general condition of the tree, even if inferred with an inaccurate position and dimension. This metric can be misleading if the zone of interest (positive) is very small in relation to the total, being increased due to the increase in the accuracy of the negative values (*TN*). However, for trees, the highest risk condition occurs when there is a large cavity or deteriorated zone, making the proportions more suitable for this metric.

$$Accuracy = \frac{TP + TN}{TP + FP + TN + FN} \quad (1)$$

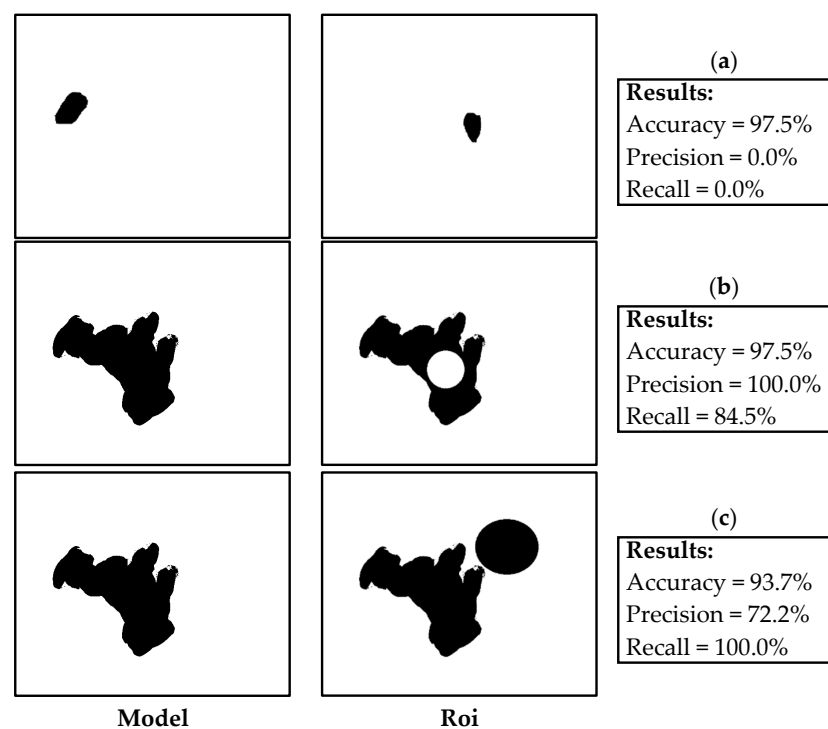


Figure 4. Example of confusion matrix results considering the zone of interest obtained from a real image (*model*) and the zone of interest obtained by tomography (*Roi*) considering conditions for better results of accuracy (a), precision (b) and recall (c).

The precision Equation (2) measures, among all the positive classifications (TP and FP) that the produced image indicated, how many are correct (TP). In the example (Figure 4b), the accuracy is 100%, although there is an unfilled zone in the image (smaller spot than the model) because it does not measure the negative classifications (TN and FN), and the image does not show FP , i.e., has no points indicated as areas of interest outside the *model*. Thus, in tomography performed in a tree stem with a cavity, a high precision would indicate that the image did not infer a cavity outside the right location (*model*), which is interesting as long as the accuracy is also good because as the metric does not consider the FN s, the cavity may be undersized. Accuracy can be considered the most appropriate metric when false positives are considered more harmful than false negatives.

$$\text{Precision} = \frac{Tp}{TP + FP} \quad (2)$$

Recall in Equation (3) is a metric that measures, among all predicted positive class situations (TP and FN), how many were correct; that is, it measures whether the model was fully filled, regardless of whether there is an indication of another region with false positives in the image because they do not enter the calculation (Figure 4c). Tree tomography could indicate an oversized area of interest, which in terms of safety is better than high precision but could lead to a false indication of tree risk if the error in this metric is very high. This metric is suitable for situations in which false negatives are considered more harmful than false positives. This seems to be the case for tree inspections since the most important task is to find cavities or deteriorations, even if some healthy parts are erroneously classified as containing one of these conditions.

$$\text{Recall} = \frac{Tp}{TP + FN} \quad (3)$$

The harmonic mean Equation (4) is closer to the lower values than the simple mean, making it a metric that, when it has low values, indicates that either the precision or the recall is low.

$$\text{F1 score} = 2 \frac{\text{precision} \times \text{recall}}{\text{precision} + \text{recall}} \quad (4)$$

The calculations were performed using the Python script proposed by [16]. A comparison was made for each disc isolating the condition of the region of interest (Ca or Ca+ Bio) obtained from the photograph (*model*) or from the tomographic image (*Roi*) (example in Figure 5). Before the comparison, the images underwent dimensional adaptation using *ImageJ* software so they would have the same number of pixels. In addition to the two images to be compared (*model* and *Roi*), the confusion matrix requires a third image called internal points, which is also obtained from the tomographic image, selecting only the contour and thus delimiting the field to be used in the comparison (example in Figure 5). As one of the research objectives was to find the most appropriate range to infer regions with cavities (Ca) and regions with cavities and biodeterioration (Ca+Bio), the comparisons were made with the tomographic images constructed with each level of % V_{max} , and for each comparison, the metrics of the confusion matrix (accuracy, precision, recall and F1 score) were calculated. These analyses were performed for the images constructed using each of the three interpolators (ISD, ME without and with compensation) and under both conditions (using a filter and without using a filter), resulting in the comparison of 3024 images.

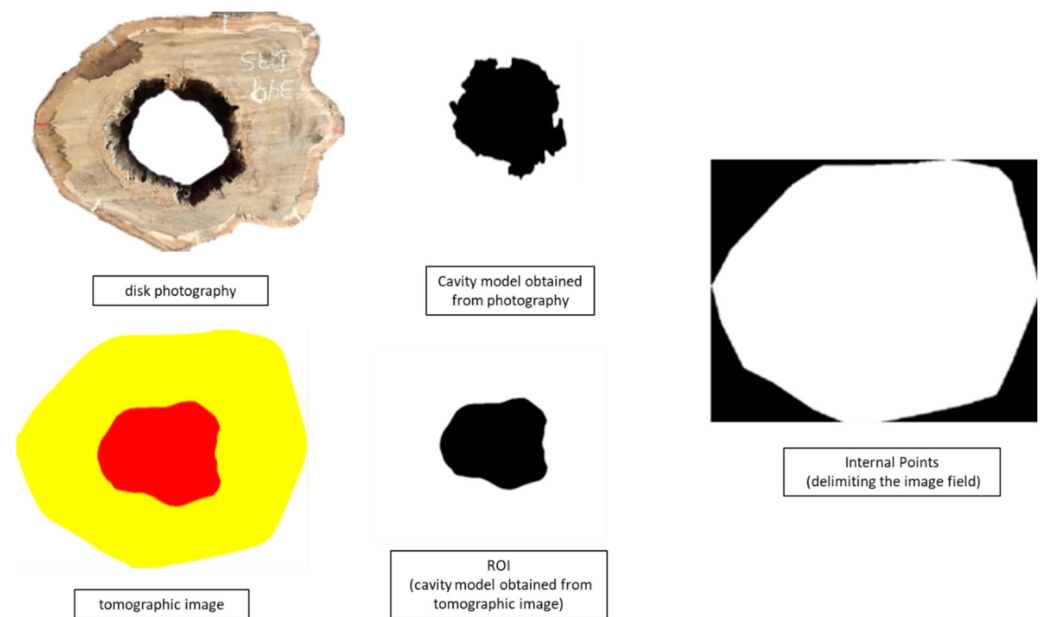


Figure 5. Example of images used in the confusion matrix to calculate the metrics.

2.2.6. Calculation of the Percentages of the Lengths of the Theoretical Routes Passing through Zones of Interest

The mesh with the theoretical wave propagation routes was projected in the disc photographs (example in Figure 6), which were created in ImageJ software using a known distance between two points to change the scale from pixels to centimeters. In the same software, the tools Straight Line and Measure were used to calculate, for each theoretical route, the lengths (L) of the sections that passed through zones of interest, which in this study were the intact, deteriorated or cavity regions. With these data, the percentage of the theoretical route that was within intact wood, within deteriorated wood or within cavities was calculated. To facilitate the analysis, for each zone of interest (intact, cavity or biodeterioration), ten percentage intervals of the route length (L) containing these zones were considered: $L = 100\%$; $90\% \leq L < 100\%$; $80\% \leq L < 90\%$; $70\% \leq L < 80\%$; $60\% \leq L < 70\%$; $50\% \leq L < 60\%$; $40\% \leq L < 50\%$; $30\% \leq L < 40\%$; $20\% \leq L < 30\%$; $10\% \leq L < 20\%$; and $L < 10\%$. The speeds in each route were referenced to the maximum speed obtained in all routes of the loop ($\% V_{\max}$).



Figure 6. Example of theoretical routes of the projected measurement mesh on the face of the disc.

2.2.7. Evaluation of Results

The first part of the analysis, with details of the theoretical measurement routes, verifies the coherence of $\% V_{\max}$ behavior as a function of the condition of the theoretical section covered. For this, regression analysis was used, seeking the statistical model that best

suited the behavior of % Vmax as a function of the wave path condition. This analysis was performed using a tool named “Regression Model Selection” available in statistical software (Statgraphics Centurion XV version 15.1.02). The procedure used by this tool considers all possible regressions involving different combinations of the independent variables. It compares models based on the adjusted R-Squared, Mallows’ Cp statistic, and the mean squared error. This analysis is purely theoretical since when we make an inspection, we do not have advance knowledge of the sections traveled by the wave. Additionally, we know that the wave propagation route is only theoretical since there are deviations due to various causes, as previously mentioned. However, this analysis allows for evaluating the coherence of the general behavior of the influence of cavities and biodeteriorations on the propagation speed of ultrasound waves, in addition to being able to serve as a basis for further studies.

The second part of the analysis focuses on the metrics of the confusion matrix. Considering all the aspects presented in the introduction, we find that the choice of the metric should be made according to the specificity of the study. For this study, we analyzed the metrics to obtain the most appropriate % Vmax to infer zones of interest (Ca and Ca+Bio). For this, we evaluated the influence of % Vmax (every 5%) adopted to infer the condition of the wood (Ca and Ca+Bio) on the behavior of each metric, seeking its maximum values. The image comparisons were also used to evaluate the different interpolators and the possible use of the filter.

2.2.8. Range Validation

To validate the cutting speed ranges obtained for the inference of Ca and Ca+Bio in the species used as a case study, as well as the interpolator and the use of a filter, an image with three colors was generated to represent the inference ranges Ca, Ca+Bio and intact wood.

3. Results

3.1. Behavior of Ultrasound Wave Propagation Velocity in Different Theoretical Measurement Routes

As expected, as the percentage of intact wood (L_i) decreases within the theoretical route, the % Vmax also decreases, and it was possible to obtain a statistically significant (P value = 0.000) model (Squared Root-X) with a 95% confidence level, which represents this variation and explains 98% of the variability in maximum speed percentage (Figure 7).

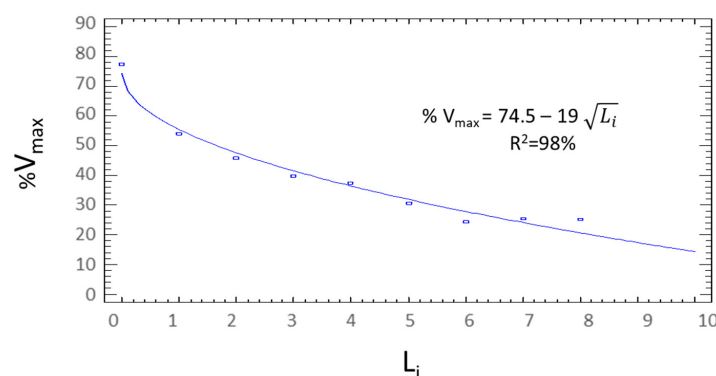


Figure 7. Behavior of the average percentage of the maximum speed as a function of the percentage interval of the path length within the intact zone (L_i), represented by a Squared Root-X model. Legend: L_i = 100% of the interval = 0; L_i between 91% and 100% of the interval = 1; L_i between 80% and 90% of the interval = 2; L_i between 70% and 80% of the interval = 3; L_i between 60% and 70% of the interval = 4; L_i between 50% and 60% of the interval = 5; L_i between 40% and 50% of the interval = 6; L_i between 30% and 40% of the interval = 7; L_i between 20% and 30% of the interval = 8; L_i between 10% and 20% of the interval = 9; and L_i < 10% of the interval = 10.

A statistically significant (p value = 0.0083) correlation model (Squared-X), with a 95% safety level, was obtained between the % Vmax and the percentage of deteriorated zones (L_d) within the theoretical route, with a correlation coefficient $R = 0.83$ and coefficient of determination $R^2 = 69\%$ (Figure 8).

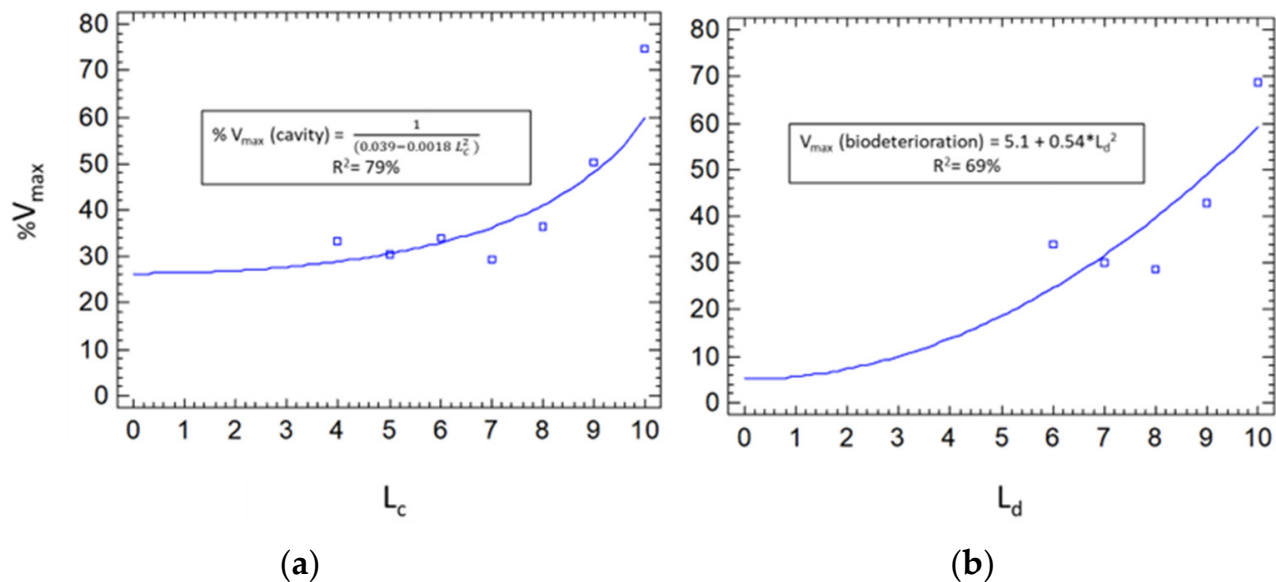


Figure 8. Behavior of the average percentage of the maximum velocity as a function of the percentage interval of the path length within the zones with cavity (a) represented by Reciprocal-Y Squared-X model and biodeterioration (b) represented by a Squared-X model. Legend: Lc (percentage of the path length within the zones with cavity) or Ld (percentage of the path length within the zones with biodeterioration) = 100% of the interval = 0; Lc or Ld between 91% and 100% of the interval = 1; Lc or Ld between 80% and 90% of the interval = 2; Lc or Ld between 70% and 80% of the interval = 3; Lc or Ld between 60% and 70% of the interval = 4; Lc or Ld between 50% and 60% of the interval = 5; Lc or Ld between 40% and 50% of the interval = 6; Lc or Ld between 30% and 40% of the interval = 7; Lc or Ld between 20% and 30% of the interval = 8; Lc or Ld between 10% and 20% of the interval = 9; and Lc or Ld < 10% of the interval = 10.

For wood with cavities, a statistically significant (p -value = 0.0072) correlation model (Reciprocal-Y Squared-X) was also obtained, with a 95% safety level, between the % Vmax and the percentage of zones with cavities (L_c) within the theoretical route with $R^2 = 79\%$ (Figure 8).

3.2. Inference of Velocity Ranges for the Detection of Deteriorated Zones or Cavities Using the Metrics of the Confusion Matrix

An evaluation of the behavior of the confusion matrix metrics as a function of the maximum velocity percentage intervals indicates that the recall is not an adequate metric to define the most appropriate interval for the inference of zones with cavities or with cavities plus biodeteriorations (objective of the research) because the maximum point for all algorithms, regardless of the application of the filter, occurred for 100% Vmax (Figure 9).

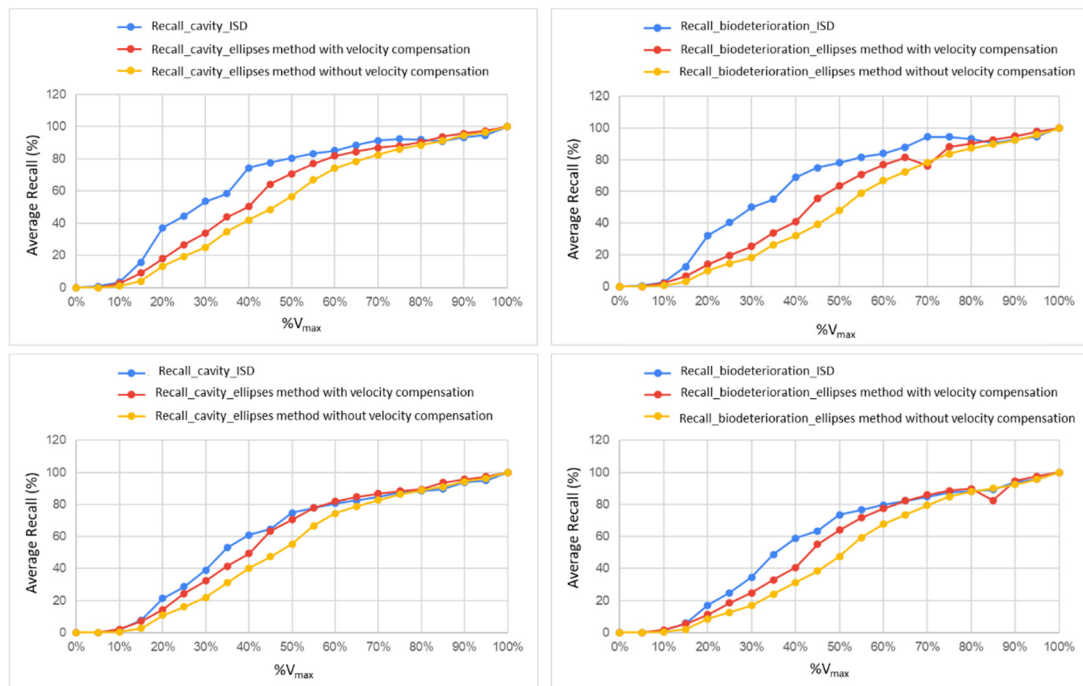


Figure 9. Behavior of the recall metric obtained with the application of the confusion matrix for the cavity and the cavity plus biodeterioration as zones of interest, without the application of filters (upper graphs) and with the application of filters (lower graphs).

The accuracy metric was practically the same for the Ellipses algorithms with and without compensation and with or without the application of a filter (Figure 10). The use of filters in images generated with the ISD algorithm showed better results (Figure 11), reflecting on the accuracy results (Figure 10).

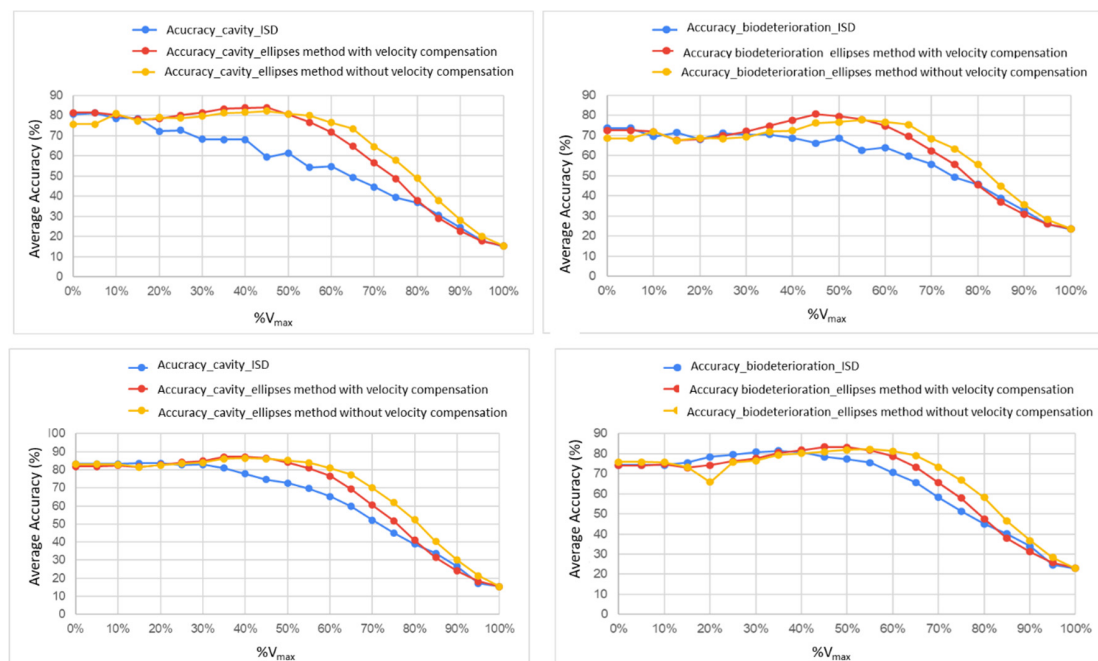


Figure 10. Behavior of the accuracy metric obtained with the application of the confusion matrix for the cavity and the cavity plus biodeterioration as zones of interest, without the application of filters (upper graphs) and with the application of filters (lower graphs).

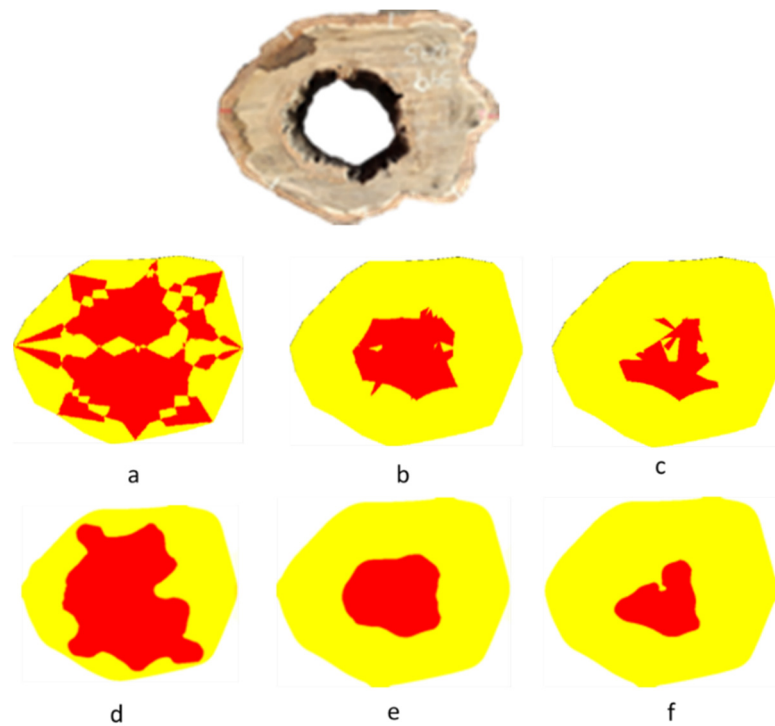


Figure 11. Example of disc photography and tomographic images obtained without filter application with ISD algorithms (a), Ellipses with compensation (b) and Ellipses without compensation (c) and with filter application with ISD algorithms (d), Ellipses with compensation (e) and Ellipses without compensation (f).

The behavior of the precision and F1 score metrics given by the graphics were similar for all algorithms and compared with each other (Figures 12 and 13).

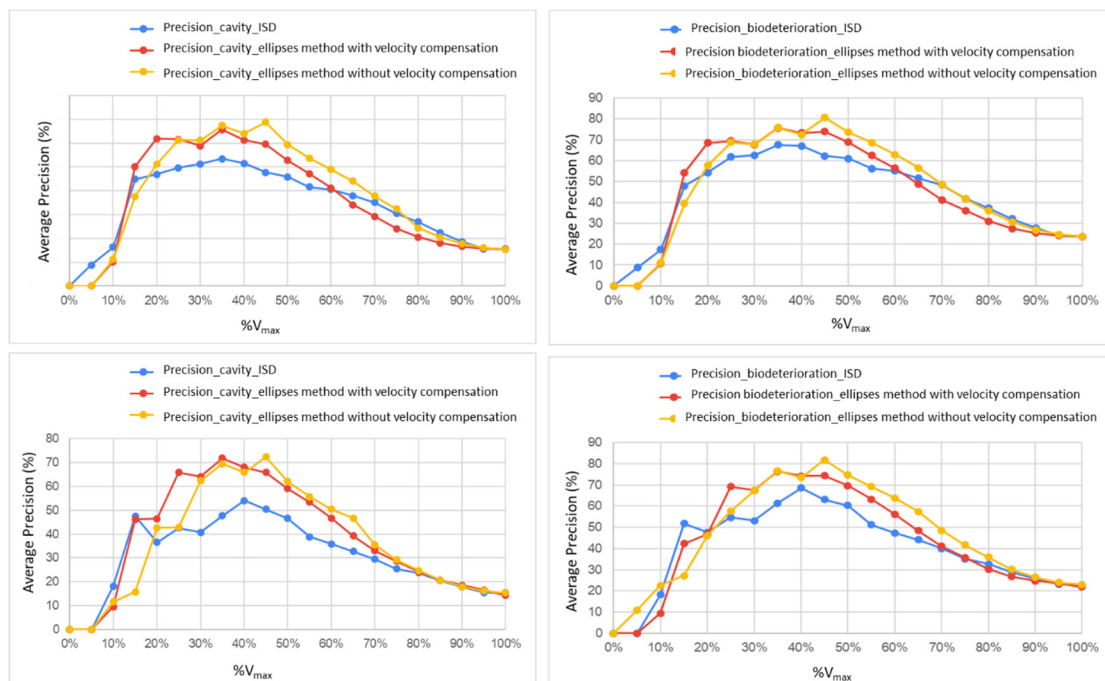


Figure 12. Behavior of the precision metric, obtained with the application of the confusion matrix for the cavity and the cavity plus biodeterioration as zones of interest, without the application of filters (upper graphs) and with the application of filters (lower graphs).

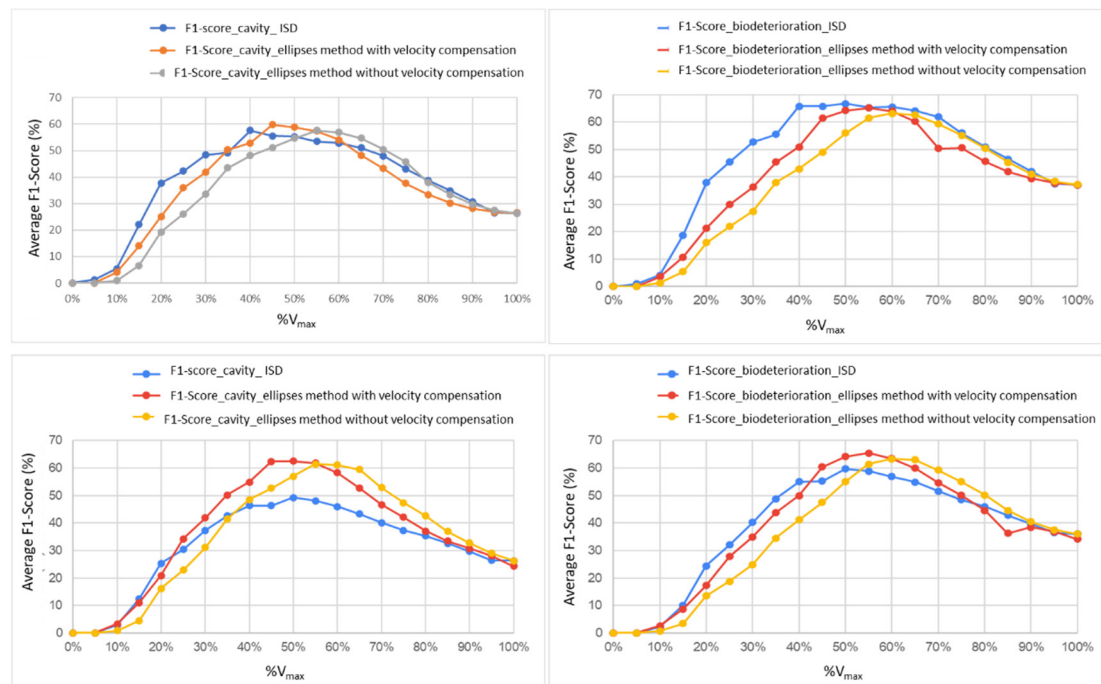


Figure 13. Behavior of the F1 score metric, obtained with the application of the confusion matrix for the cavity and cavity plus biodeterioration as zones of interest, without application of filters (upper graphs) and with the application of filters (lower graphs).

Tables 3–5 show the maximum percentages of the metrics of the confusion matrix with respective percentages of the maximum velocity (% V_{max}) obtained for zones of interest (cavity—Ca or cavity plus biodeterioration—Ca+Bio), using or not using filters in the images and for each interpolation algorithm.

Table 3. Maximum percentages of the metrics of the confusion matrix and respective percentages of the maximum velocity (% V_{max}) obtained for zones of interest (cavity—Ca or cavity plus biodeterioration—Ca+Bio), using or not using filters in the images. Interpolation algorithm: ISD.

Filter	Condition/Metrics	Metric (%) and (% V_{max})			
		Accuracy	Precision	Recall	F1 Score
Without	Ca	81.3 (5)	53.5 (35)	100.0 (100)	57.0 (40)
	Ca+Bio	71.4 (15)	67.5 (35)	100.0 (100)	66.6 (50)
With	Ca	83.7 (15)	54.0 (40)	100.0 (100)	49.0 (50)
	Ca+Bio	81.5 (35)	68.6 (40)	100.0 (100)	66.6 (50)

Table 4. Maximum percentages of the metrics of the confusion matrix and respective percentages of the maximum velocity (% V_{max}) obtained for zones of interest (cavity—Ca or cavity plus biodeterioration—Ca+Bio), using or not using filters in the images. Interpolation algorithm: Ellipses without compensation.

Filter	Condition/Metrics	Metric (%) and (% V_{max})			
		Accuracy	Precision	Recall	F1 Score
Without	Cavity	82.0 (45)	67.4 (35)	100.0 (100)	57.6 (55)
	Biodeterioration	77.8 (55)	80.7 (45)	100.0 (100)	63.2 (60)
With	Cavity	86.5 (40)	72.4 (45)	100.0 (100)	61.4 (55)
	Biodeterioration	82.3 (55)	81.9 (45)	100.0 (100)	63.4 (60)

Table 5. Maximum percentages of the metrics of the confusion matrix and respective percentages of the maximum velocity (% V_{max}) obtained for zones of interest (cavity—Ca or cavity plus biodeterioration—Ca+Bio), using or not using filters in the images. Interpolation algorithm: Ellipses with compensation.

Filter	Condition/Metrics	% Metric and (% V_{max})			
		Accuracy	Precision	Recall	F1 Score
Without	Cavity	84.0 (45)	65.6 (35)	100.0 (100)	59.8 (45)
	Biodeterioration	80.7 (45)	75.7 (35)	100.0 (100)	65.2 (55)
With	Cavity	87.2 (40)	71.8 (35)	100.0 (100)	62.5 (50)
	Biodeterioration	83.3 (45)	76.4 (35)	100.0 (100)	65.5 (55)

Based on the results from Tables 3–5, the metrics were then evaluated adopting velocities up to 40% of the maximum velocity for cavity inference and up to 45% for cavity plus biodeterioration (Table 6).

Table 6. Metrics obtained for the different algorithms and application or not of filter in the construction of the images, adopting speeds up to 40% of the maximum speed for cavity inference and up to 45% of the maximum speed for cavity inference plus biodeterioration.

Filter	Condition	Metric (%)			
		Accuracy	Accuracy	Recall	F1 Score
Algorithm: Ellipses with compensation					
With	Cavity	87.2	68.1	49.4	54.9
	Biodeterioration	83.3	74.4	55.1	60.4
Without	Cavity	83.9	61.3	50.3	52.8
	Biodeterioration	80.7	74.0	55.4	61.4
Algorithm: Ellipses without compensation					
With	Cavity	86.5	65.8	40.2	48.5
	Biodeterioration	81.0	81.9	38.4	47.5
Without	Cavity	81.6	64.0	42.1	48.1
	Biodeterioration	76.3	80.7	39.2	49.1
Algorithm: ISD					
With	Cavity	77.9	54.0	60.8	46.4
	Biodeterioration	78.5	63.1	63.4	55.3
Without	Cavity	68.2	51.6	74.3	57.6
	Biodeterioration	66.2	62.3	75.1	65.7

3.3. Validation

Images were constructed using the cutting velocity ranges obtained with the methodology applied to the *Sibipiruna* species (up to 40% V_{max} for Ca inference, up to 45% V_{max} for Ca+Bio inference and above 45% V_{max} for intact wood inference), and the ME with compensation as interpolator and the median filter with 25 pixels allowed evaluation of the reach of the proposed methodology (example in Figure 14).

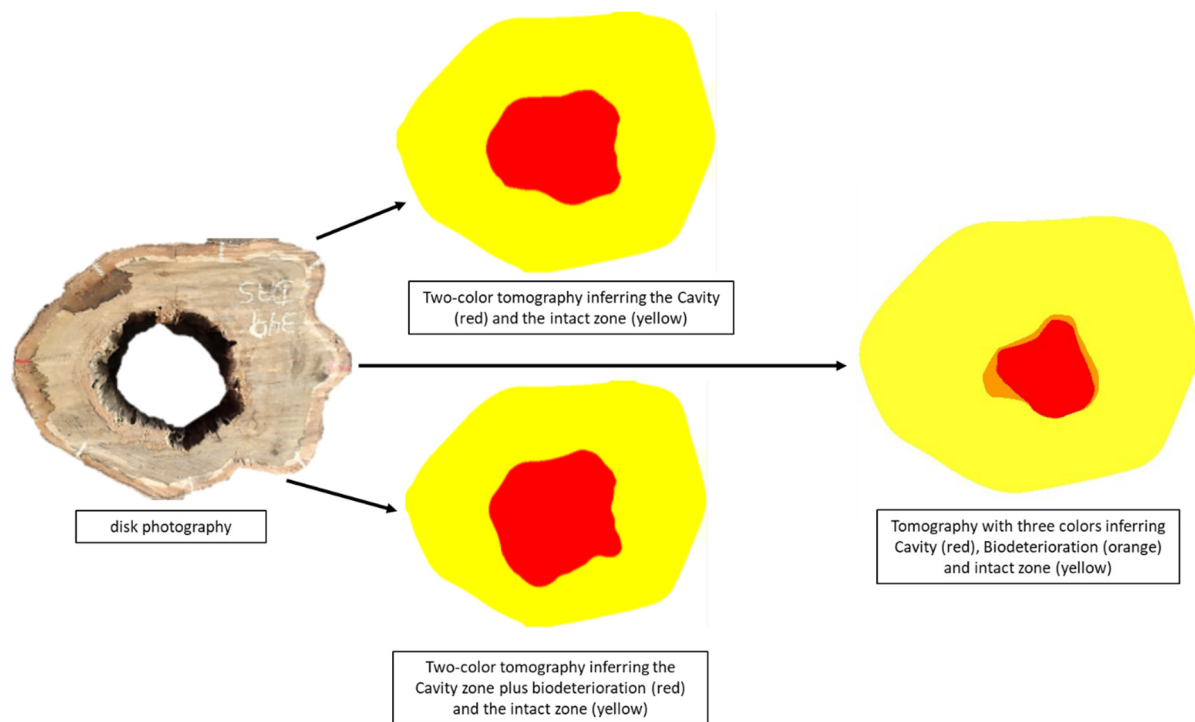


Figure 14. Example of the process with disk photography, tomographic images produced with two colors and cutting velocity for Ca inference (up to 40%) and for Ca+Bio inference (up to 45%) and tomographic image with three colors separating Ca from Ca+Bio.

4. Discussion

4.1. Behavior of Ultrasound Wave Propagation Velocity in Different Theoretical Measurement Routes

In the measurement routes that passed through intact wood only ($L_i = \text{zero interval}$ in Figure 7), the average percentage of the maximum velocity was 77%, indicating that, even in wood without deterioration or cavities, there is velocity variation. This behavior is expected because wood is a heterogeneous and orthotropic material, and the routes pass through different regions of the stem (heartwood and sapwood) and with different slopes in relation to the growth rings (tangential, radial and mixed), with deviations from the expected theoretical route [13]. Even without any internal defect, [13] obtained an average variation of 23% in the velocity of stress wave propagation in the theoretical measurement routes with higher speeds in the radial routes and lower speeds in the tangential edge routes. The authors adopted a quadratic equation to represent the behavior of the propagation velocity of stress waves as a function of the angle formed by the theoretical measurement route and the radial direction.

For deteriorated wood, only conditions of routes classified in the ranges from range 6 ($40\% \leq L_d < 50\%$) were sampled (Figure 8). The behavior of the velocity variation indicated that up to range 8 ($20\% \leq L_d < 30\%$), the velocities were practically constant and approximately 30% V_{max} (Figure 8). For range 9 ($10\% \leq L_d < 20\%$), the velocity rose to 43% V_{max} , and in range 10 ($L_d < 10\%$), it reached an average of 69% V_{max} (Figure 8). The lengths with deterioration in the routes ranged from 4.3 mm to 223 mm.

For wood with cavities, we had only path conditions classified from range 4 ($60\% \leq L_c < 70\%$) (Figure 8). In this case, it is observed that, until range 7 ($30\% \leq L_c < 40\%$), the velocities were practically constant and approximately 30% of the maximum velocity (Figure 8). For ranges 8 ($20\% \leq L_c < 30\%$) and 9 ($10\% \leq L_c < 20\%$), the velocity was approximately 50% of the maximum, and in range 10 ($L_c < 10\%$), it reached an average of 75%, only slightly below what was obtained in 100% intact wood (77%) (Figure 7). The lengths with cavities in the routes ranged from 5.2 mm to 310 mm.

4.2. Inference of Velocity Ranges for the Detection of Deteriorated Zones or Cavities Using the Metrics of the Confusion Matrix

The behavior obtained for the recall metric occurs because the calculation of this metric Equation (3) does not consider the false positives, and therefore, for 100% V_{\max} , the entire disc will be considered a zone of interest and thus be completely filled. This means that for the confusion matrix, all pixels of the produced image will be positive; therefore, many of them are false positives (FPs) but not false negatives (FNs), and because false positives do not enter the calculation, the metric value will be 100%.

For the accuracy, there is an initial stretch with practically constant values for the metric, but slightly ascending, so there is a maximum value (approximately 40% to 50% V_{\max} for Ca and Ca+Bio, respectively) from which the values are decreasing (Figure 10). For these algorithms, there is an initial stretch with practically constant values for the metric, but slightly ascending, so there is a maximum value (approximately 40% to 50% V_{\max} for Ca and Ca+Bio, respectively) from which the values are decreasing (Figure 10). For the ISD without the filter application, this level of approximately constant values practically does not exist (Figure 10), so the maximum value of the metric is obtained with very low percentages of the maximum velocity (between 5% and 15% for Ca and Ca+Bio, respectively). When the filter is applied, the ISD behavior is similar to that of the other algorithms (Figure 10), but the peaks occur at lower percentages (approximately 30% to 40% V_{\max}). This result indicates that the filter has a greater effect for the ISD than for the other algorithms, confirming what can be observed visually by comparing the images generated without a filter with those generated with a filter (Figure 11), indicating that the images generated by the ISD exhibit higher interference.

For the precision metric, there is a more evident peak in the behavior of the curve that represents the value of the metric (%) versus the value of the % V_{\max} adopted to represent the zone of interest (Figure 12). Although the peaks were not numerically equal, the behavior of the graph was similar for all algorithms.

Considering the inadequate behavior of the recall metric, the use of the F1 score metric to define the most appropriate interval for the inference of the zones will also not be feasible since it is a combination of the precision and recall metric results of Equation (4). The behavior of the graph for the F1 score metric (Figure 13) is similar to that of precision and, because it is a combination of the precision and recall metrics, this indicates that the linear and increasing behavior of recall affected the final behavior of the metric less than precision. The difference between the precision and F1 score metrics is that because the ISD algorithm generally expands the size of the area of interest, the F1 score tends to have higher values for the ISD (Figure 13), while for the accuracy, a metric in which the false positive is included in the calculation Equation (2), the ISD is, in general, always less than the other metrics (Figure 12).

For all algorithms, the application of the filter in the images improved the maximum values of the metrics, in the analysis of both of the Ca and Ca+Bio zones. This result confirms that the applied filter reduces interference caused by the interpolation systems in the images, as observed by [19].

Considering the behavior of the recall metric and, consequently, the F1 score metric, they were not included in the analysis of the % V_{\max} ranges most appropriate for the inference of Ca and Ca+Bio, leaving the accuracy and precision metrics.

For the ISD interpolation algorithm, only the accuracy (without and with filter) showed different maximum metric values for % V_{\max} for Ca and Ca+Bio (Table 2). The precision metric did not differentiate the zones of interest (Ca from Ca+Bio). In addition, as previously discussed, the behavior of the graph (Figure 10), especially without the application of a filter, shows a decreasing linear trend, with the peak of % V_{\max} indicative of the very low zones of interest (5% and 15%) (Table 3).

For the ME without compensation, the accuracy and precision differentiated the % V_{\max} for Ca and Ca+Bio when there was no application of filters, and with the application

of the filter, only the accuracy allowed differentiation (Table 4). In the case of this metric, the % V_{\max} is between 40% and 55% (Table 4).

For the ME with compensation, differentiation occurred only for the accuracy and with the application of a filter in the construction of the image, with % V_{\max} between 40% and 45% (Table 5).

From the analysis, we found that the accuracy metric was the one that differentiated the regions of interest (Ca and Ca+Bio) and presented the highest values for all algorithms. The highest metric value (87.2%) was obtained for the Ellipse algorithm with compensation and with the application of a filter in the construction of the image. Considering the results obtained in this study, it is assumed that, for Sibipiruna (used as a case study), the best range of % V_{\max} for the inference of cavities in ultrasonic tomography is from 0 to 40% and, for the inference of added cavities of biodeterioration, up to 45%. Applying these percentages to all filter conditions and algorithms studied, it is found that the best results, considering the accuracy and precision metrics, are for Ellipse algorithms with and without compensation (Table 6). The application of the filter, although always leading to increased metrics, is particularly important for the ISD algorithm (Table 6). A comparison of these metrics when applied to tomographic images with the literature is difficult because these studies remain scarce. The authors of [16] obtained accuracies of 94.3% and 93.5% using discs with artificially produced cavities at one end and two ends of the disc, respectively. In these same discs, [16] obtained precision values of 30.8% and 53.8% and recall values of 45.6% and 71.7%, respectively. The values obtained in this study, with actual discs and deteriorations, were generally lower for accuracy and recall but higher for precision (Table 6).

5. Conclusions

- The proposed methodology allowed us to obtain the intended results, and the application in the species used as a case study (Sibipiruna) led to the conclusion that the most appropriate speed range for inference of the cavity reached 40% V_{\max} , and for a cavity associated with biodeterioration, it reached 45% V_{\max} .
- The interpolator with the best results was the Ellipses method with compensation.
- The use of a median filter improved the quality of the images produced using any of the interpolation methods, which is necessary when the interpolator is the inverse of the square of distance (ISD).
- Accuracy was the most appropriate metric for evaluating image quality when the zone of interest is the defect.

Author Contributions: Conceptualization, R.G. and S.S.S.A.P.; methodology, R.G., S.S.S.A.P. and M.N.d.R.; validation, R.G. and S.S.S.A.P.; investigation, S.S.S.A.P. and M.N.d.R.; resources, R.G.; writing—original draft preparation, R.G. and S.S.S.A.P.; writing—review and editing, R.G. All authors have read and agreed to the published version of the manuscript.

Funding: This research was funded by CNPq (National Council for Scientific and Technological Development)—Proc. 141067-2018-7 (scholarship) and Proc. 426130/2018-9 (research) and CAPES (Coordination for the Improvement of Higher Education)—Finance Code 001 and Proc. 88887.467257/2019-00 (scholarship and internship in Spain).

Data Availability Statement: The data supporting reported results can be found, including links to publicly archived datasets generated during the study, at the University repository (available after the paper is approved).

Acknowledgments: The authors thank the CNPq for the scholarship (Proc. 141067-2018-7) and funding of the research (Proc. 426130/2018-9), the Coordination for the Improvement of Higher Education (CAPES) for the scholarship and internship in Spain (Process—88887.467257/2019-00), and the Foundation for Research Support of the State of São Paulo (Fundação de Amparo a Pesquisa do Estado de São Paulo—FAPESP) for funding research from LabEND, with which it was possible to purchase all the equipment used in the research. We also thank *Carlos Eduardo Bento* (student of the Service of Student Support (SAE) of the Graduate Pro-Rector (PRG) of UNICAMP) for the support in the laboratory tests and *José Victor Gonçalves Cardoso* (CNPq scholarship in the project Proc. 426130/2018-9) for support related to the analysis of the measurement routes.

Conflicts of Interest: The authors declare no conflict of interest.

References

- Conway, T.M. Tending their urban forest: Residents' motivations for tree planting and removal. *Urban For. Urban Green.* **2016**, *17*, 23–32. [\[CrossRef\]](#)
- Arciniegas, A.; Prieto, F.; Brancheriau, L.; Lasaygues, P. Literature review of acoustic and ultrasonic tomograph in standing trees. *Trees* **2014**, *28*, 1559–1567. [\[CrossRef\]](#)
- Wu, X.; Li, G.; Jiao, Z.; Wang, X. Reliability of acoustic tomography and ground-penetrating radar for tree decay detection. *Appl. Plant Sci.* **2018**, *6*, e1187. [\[CrossRef\]](#) [\[PubMed\]](#)
- Wang, X.; Wiedenbeck, J.; Liang, S. Acoustic tomography for decay detection in black cherry trees. *Wood Fiber Sci.* **2009**, *41*, 127–137.
- Gonçalves, R.; Reis, M.N.; Ziller, D.P.; Palma, S.S.A. Ultrasonic tomography in logs of urban trees with different levels and types of hollows. In Proceedings of the 20th International Nondestructive Testing and Evaluation of Wood Symposium, Madison, MI, USA, 12–15 September 2017.
- Brancheriau, L.; Ghodrati, A.; Gallet, P.; Thaunay, P.; Lasaygues, P. Application of ultrasonic tomography to characterize the mechanical state of standing trees (*Picea abies*). *J. Phys. Conf. Ser.* **2012**, *353*, 012007. [\[CrossRef\]](#)
- Bucur, V. Ultrasonic techniques for nondestructive testing of standing trees. *Ultrasonics* **2005**, *43*, 237–239. [\[CrossRef\]](#)
- Socco, L.V.; Sambuelli, L.; Martinis, R.; Comino, E.; Nicolotti, G. Feasibility of ultrasonic tomography for nondestructive testing of decay on living trees. *Res. Nondestruct. Eval.* **2004**, *15*, 31–54. [\[CrossRef\]](#)
- Nicolotti, G.; Socco, L.V.; Martinis, R.; Godio, A.; Sambuelli, L. Application and comparison of three tomographic techniques for detection of decay in trees. *J. Arboric* **2003**, *29*, 66–78. [\[CrossRef\]](#)
- Divos, F.; Divos, P. Resolution of stress wave based on acoustic tomography. In Proceedings of the 14th International Symposium on Nondestructive Testing of Wood, Eberswalde, Germany, 2–4 May 2005.
- Bucur, V. Acoustics of Wood (Second Edition). *J. Acoust. Soc. Am.* **2006**, *119*, 3506. [\[CrossRef\]](#)
- Palma, S.S.A.; Gonçalves, R.; Trinca, A.J.; Costa, C.P.; Guerra, M.N.R.; Martins, G.A. Interference from knots, wave propagation direction and effect of juvenile and reaction wood on velocities in ultrasound tomography. *BioResources* **2018**, *13*, 2834–2845. [\[CrossRef\]](#)
- Wei, X.; Xu, S.; Sun, L.; Tian, C.; Du, C. Propagation velocity model and two-dimensional defect imaging of stress wave in Larch (*Larix gmelinii*) wood. *Bioresources* **2021**, *16*, 6799–6813. [\[CrossRef\]](#)
- Gonçalves, R.; Costa, O.L. Influence of moisture content on longitudinal, radial, and tangential ultrasonic velocity for two Brazilian wood species. *Wood Fiber Sci.* **2008**, *40*, 580–586.
- Wang, X.; Divos, F.; Pilon, C.; Brashaw, B.K.; Ross, R.J.; Pellerin, R.F. *Assessment of Decay in Standing Timber Using StressWave Timing Non-Destructive Evaluation Tools: A Guide for Use and Interpretation*; General Technical Report (GTR), FPL-GTR-147; Department of Agriculture, Forest Service, Forest Products Laboratory: Madison, WI, USA, 2004; 12p.
- Strobel, J.R.A.; Carvalho, M.A.G.; Gonçalves, R.; Pedroso, C.B.; Reis, M.N.; Martins, P. Quantitative image analysis of acoustic tomography in woods. *Eur. J. Wood Wood Prod.* **2018**, *76*, 1379–1389. [\[CrossRef\]](#)
- Du, X.; Li, S.; Li, G.; Feng, H.; Chen, S. Stress wave tomography of wood internal defects using ellipse-based spatial interpolation and velocity compensation. *BioResources* **2015**, *10*, 3948–3962. [\[CrossRef\]](#)
- Feng, H.; Li, G.; Fu, S.; Wang, X. Tomographic image reconstruction using an interpolation method for tree decay detection. *BioResources* **2014**, *9*, 3248–3263. [\[CrossRef\]](#)
- Palma, S.S.A.; Gonçalves, R. Tomographic images of the trunks generated using ultrasound and post-processed images: Influence of the number of measurement points. *BioResources* **2022**, *17*, 6638–6655. [\[CrossRef\]](#)
- Espinosa, L.; Brancheriau, L.; Cortes, Y.; Prieto, F.; Lasaygues, P. Ultrasound computed tomography on standing trees: Accounting for wood anisotropy permits a more accurate detection of defects. *Ann. For. Sci.* **2020**, *77*, 68. [\[CrossRef\]](#)
- Reis, M.N.; Gonçalves, R.; Brazolin, S.; Palma, S.S.A.; Pereira, R.G.F.N.B. Reliability of tomographic image to represent variation in stem wood properties assessed using confusion matrix metrics. *Wood Sci. Technol.* **2022**, *56*, 921–945. [\[CrossRef\]](#)
- Reis, M.N.; Gonçalves, R.; Brazolin, S.; Palma, S.S.A. Strength loss inference due to decay or cavities in tree trunks using tomographic imaging data applied to equations proposed in the literature. *Forests* **2022**, *13*, 596. [\[CrossRef\]](#)
- Trinca, A.J.; Gonçalves, R.; Lino, A.C.L.; Silva, M.V.G. Use of Laser to Determine Profile of Trees. In Proceedings of the 18th International Nondestructive Testing and Evaluation of Wood, Madison, WI, USA, 24–27 September 2013.

-
24. Schubert, S.; Gsell, D.; Dual, J.; Motavalli, M.; Niemz, P. Acoustic wood tomography on trees and the challenge of wood heterogeneity. *Holzforschung* **2009**, *63*, 107–112. [[CrossRef](#)]
 25. Lin, C.J.; Kao, Y.C.; Lin, T.T.; Tsai, M.J.; Wang, S.Y.; Lin, L.D.; Wang, Y.N.; Chan, M.H. Application of an ultrasonic tomographic technique for detecting defects in standing trees. *Int. Biodeterior. Biodegrad.* **2008**, *62*, 434–441. [[CrossRef](#)]
 26. Deflorio, G.; Fink, S.; Schwarze, F.W.M.R. Detection of incipient decay in tree stems with sonic tomography after wounding and fungal inoculation. *Wood Sci. Technol.* **2008**, *42*, 117–132. [[CrossRef](#)]
 27. Fawcett, T. An introduction to ROC analysis. *Pattern Recognit. Lett.* **2006**, *27*, 861–874. [[CrossRef](#)]